Mapping and evaluating kinematics and stress/strain field at active faults and fissures: a comparison between field and drone data at NE Rift, Mt Etna (Italy)

Alessandro Tibaldi[1,2]*, Noemi Corti[1], Emanuela De Beni[3], Fabio Luca Bonali[1,2], Susanna Falsaperla[3], Horst Langer[3], Marco Neri[3], Massimo Cantarero[3], Danilo Reitano[3], Luca Fallati[1]

[1] *Department of Earth and Environmental Sciences, University of Milan-Bicocca, Milan, Italy*
[2] *CRUST- Interuniversity Center for 3D Seismotectonics with Territorial Applications, Italy*
[3] *Istituto Nazionale di Geofisica e Vulcanologia, Osservatorio Etneo, Sezione di Catania, Italy*

** Corresponding author: alessandro.tibaldi@unimib.it, Tel.: +390264482032*

Abstract

We collected drone data to quantify the kinematics at extensional fractures and normal faults, integrated this information with seismological data to reconstruct the stress field, and critically compared the results with previous fieldwork to assess the best practice. As key site, we analysed a sector of the North-East Rift of Mt Etna, an area affected by continuous ground deformation linked to gravity sliding of the volcano's eastern flank and dyke injections. The studied sector is characterized also by the existence of eruptive craters and fissures and lava flows. This work shows that this rift segment is affected by a series of NNE- to NE-striking, parallel extensional fractures characterized by an opening mode along an average N105.7° vector. The stress field is characterised by a σ_{Hmin} trending NW-SE. Normal faults strike parallel to the extensional fractures. The extensional strain obtained by cumulating the net offset at extensional fractures with the fault heave gives a stretching ratio of 1.003 in the northeastern part of the study area and 1.005 in the southwestern part. Given a maximum age of 1614 yr AD for the offset lavas, we obtained an extension rate of 1.9 cm/yr for the last 406 yr. This value is consistent with the slip along the Pernicana Fault System, confirming that they accommodate the sliding of the eastern flank of the volcano.

Keywords: Drone; Structure from Motion; rift; Etna; normal faults

1. Introduction

Quantifying offset at recent and active faults and other structures is fundamental to decipher the kinematics and stress/strain of deformation zones. This is a basic step for the assessment of seismic hazard (Lyakhovsky et al., 2012); it also contributes in the case of volcanic zones to the understanding of the crustal conditions that may facilitate magma ascent and thus the evaluation of volcanic hazard (Keir et al., 2006). At rift zones, the precise definition of the spreading direction and extensional rate requires the collection of a huge amount of data that must cover the whole rift extension. Since rift zones are composed of swarms of tens to hundreds normal faults and extension fractures, the collection of a statistically robust amount of data requires a heavy effort of fieldwork. Moreover, logistically complex conditions can affect the performance of fieldwork, as for example in the Eastern Africa rift system, where crustal extension rates have been frequently evaluated indirectly from plate tectonic models (Jestin et al., 1994; Chu and Gordon, 1999).

On active volcanoes, the presence of rough terrains and the possible exposition of researchers to explosive products frequently prevent optimal field surveys. These complex logistic conditions, in fact, do not permit to have a detailed evaluation of the strain field due to the difficulties to obtain a sufficiently large number of measurements along an extension fracture or a fault. In fact, only the collection of a large amount of horizontal dilation values can allow the precise reconstruction of the strain field. At faults, the reconstruction of heave and throw values requires the precise measurement of offset. Anyway, the measurement of fault slip profiles is very time-consuming and can be very difficult in the case of faults with offsets in the order of tens of meters.

In the last few years, the above-mentioned difficulties have been overcome by the use of Structure-from-Motion (SfM) photogrammetry applied to images collected by Unmanned Aerial Vehicles (UAVs or drones), in active volcano-tectonics studies (Bonali et al., 2019a, 2020; Trippanera et al., 2019; Weismüller et al., 2019) and to assess volcanic hazard (Müller et al., 2017; Darmawan et al., 2018; De Beni et al., 2019). Therefore, in this work we use this technique, which allows us to reconstruct very detailed Orthomosaics and Digital Surface Models (DSMs) of the surveyed areas. The resulting images, which can attain a resolution as precise as 1 cm, allow to collect several high-resolution structural data also in 3D, and take direct measurements of structures and morphostructures, like dilation values along faults and fractures, even using immersive Virtual Reality tools (Tibaldi et al., 2020).

The present paper has a double focus: on one side it describes new data useful for the interpretation of the activity of the NE Rift, and on the other side it aims to present a methodology useful for similar studies. We show that the UAV-supported methodology can attain a precision comparable to field surveys in areas affected by active deformation. We also wish to show that UAV surveys have a sufficient precision that may allow to quantify the increment of extensional deformation by successive, repeated surveys. For this, we selected a sector of the NE Rift, located on the northern summit part of Mt Etna (Italy) (Fig. 1), which is characterized by ongoing extensional fracturing, eruptive fissuring and normal faulting. This also contributes to improve our knowledge of this important volcanotectonic structure of Mt. Etna, where only a few structural surveys were conducted several years ago by Garduño et al. (1997) and Tibaldi and Groppelli (2002). The 2002-2003 eruption took place here accompanied by the development of new fractures and deposits, and thus a new mapping is necessary.

The area turned out to be very suitable for such studies because: i) it is not covered by vegetation due to the high altitude (2000-2500 m a.s.l.); ii) it is characterized by high deformation rates (in the order of 2 cm/yr, Tibaldi and Groppelli, 2002); iii) the deposits affected by faulting and fracturing are historic, and as a consequence the effects of erosion are negligible and structures are perfectly preserved.

2. Geological background

Mt Etna, one of the most active volcanoes on Earth, is located in a compressional environment (Lanzafame et al., 1997; Cocina et al., 1997, 1998), at the border between the African and the European Plate (Fig. 1A).

Etna volcano has a constantly opened central conduit feeding four summit craters named Voragine (VOR; formed in 1945), Northeast Crater (NEC; 1911), Bocca Nuova (BN; 1968) and Southeast Crater (SEC; 1971) (Fig. 1C). After 2007, a new large summit cone grew on the southeast flank of the SEC: the New South-East Crater (Del Negro et al., 2013; Behncke et al., 2014; Acocella et al., 2016). Eruptions from these summit craters are classified as summit eruptions (Acocella and Neri, 2003). Flank eruptions occur along radial fissures mostly on three main “rift zones”: the W Rift, the S Rift and the NE Rift (Fig. 1B)(Cappello et al., 2012). These flank (or lateral) eruptions are usually fed by shallow (1-3 km) dykes that propagate laterally from the central conduit (Acocella and Neri, 2009).

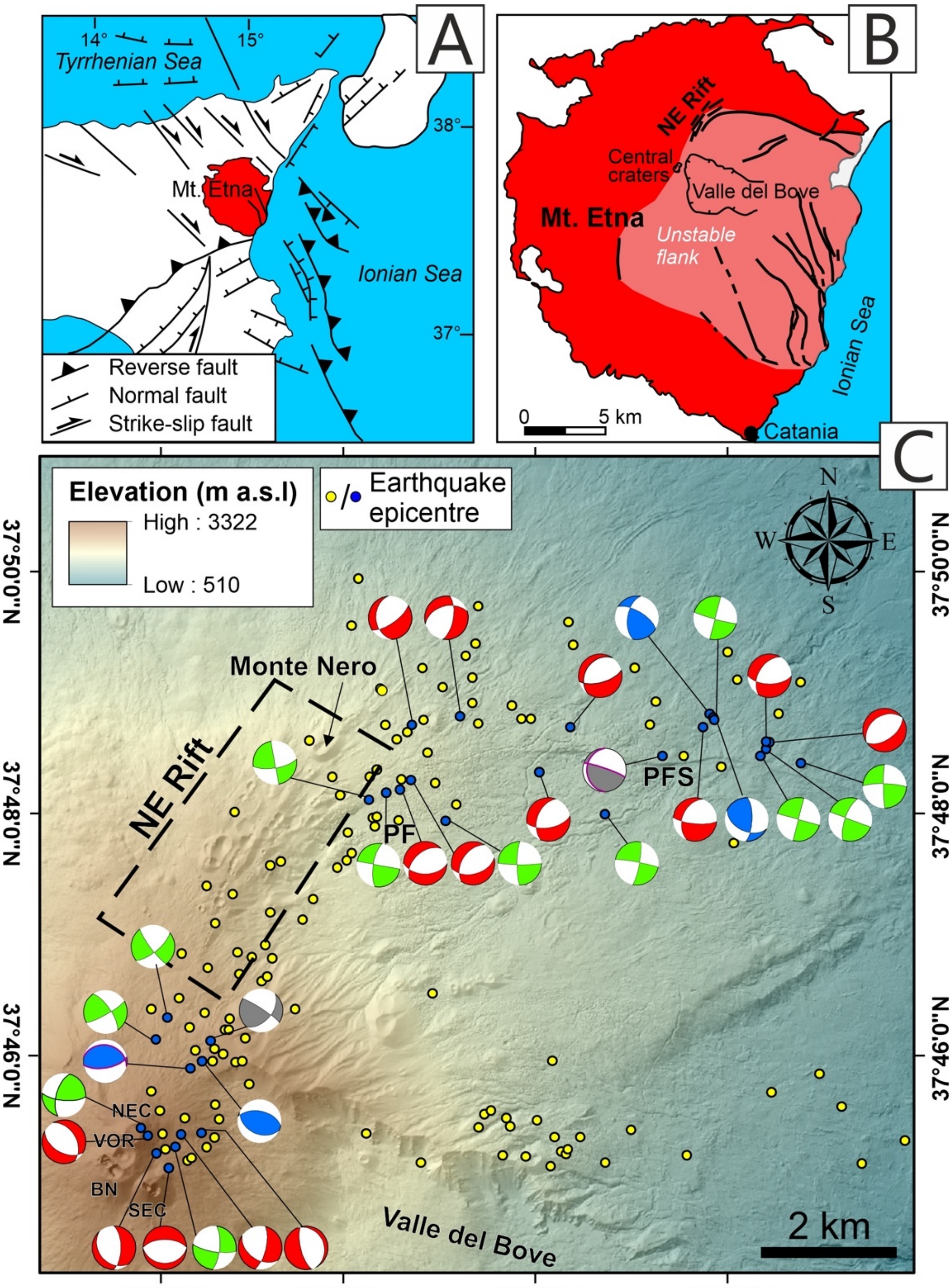

Figure 1. *(A) Map showing the geodynamic context where Etna Volcano locates; (B) Map showing the main structures of Mt Etna, with the eastern flank characterized by instability (A and B modified after Villani et al., 2020). (C) Digital Elevation Model of the upper part of Mt Etna with location of the 118 well-constrained earthquake epicenters (yellow dots) occurred during the 2002-2003 eruption (data credits: Tiziana Tuvè, INGV), and available focal mechanisms between 2008 and 2019 (blue dots) (source: http://sismoweb.ct.ingv.it/maps/eq_maps/focals/index.php). The location errors of the data set are on average 0.62 km for the epicenter and 0.41 km for the depth. Corresponding values for the median are 0.3 km (epicenter) and 0.1 km (depth). For more details on the location uncertainties, see Figs. 4 and 5 of Mostaccio et al. (2013). The black rectangle locates the area of NE Rift represented in Figures 2 and 3. PF: Piano Provenzana Fault, PFS: Pernicana Fault System, NEC: North-East Crater, VOR: Voragine Crater, BN: Bocca Nuova Crater, SEC: South-East Crater.*

The NE Rift is a network of N- to NE-striking eruptive fissures, 0.5 km wide and about 7 km long, extending from the NEC (~3320 m a.s.l.) to ~1400 m of altitude (Garduño at al., 1997) (Fig. 2). The upper portion of the rift strikes N from the summit down to 2500 m a.s.l., whereas the lower section strikes NE down to the Monte Nero area (Fig. 1C). The rift is bordered to the southeast by a 200-m-high tectonic scarp (Piano Provenzana fault, PF in Figs. 1C and 2) partially covered by recent volcanic products. To the west, the rift is limited by a small scarp, crossed by recent eruptive fissures and largely concealed by historic lava flows and cinder cones. Faults and non-eruptive fractures cut the central portion of the NE Rift; they strike between 0° and 60° and have different kinematics, including pure extension or right-lateral and left-lateral transtension (Tibaldi and Groppelli, 2002). About 35% of the fractures are associated with extrusive volcanic activity, which affected the lower portion of the same fractures: along these, hornitos, craters, small and large cinder cones are common. Moving downslope, cones and craters take on more and more a pronounced elliptical shape, with the main axis striking 30°-60°. Within them, the feeding magmatic dyke often crops out, striking 10-20° in the central part of the rift, and 40-50° in the northeastern part (Geshi and Neri, 2014).

At ~1800 m a.s.l., the NE Rift meets the 18-km-long Pernicana Fault System (PFS, Figs. 1C and 2), an active left-lateral transtensional structure bounding the unstable flank of the volcano (Groppelli and Tibaldi, 1999; Acocella and Neri, 2005). Both the NE Rift and the PFS are the NW margins of a wide sector of Etna involved in seaward displacement (Fig. 1B) (Borgia et al., 1992; Solaro et al., 2010; Ruch et al., 2010, 2013; Acocella et al., 2013; Apuani et al., 2013; Mattia et al., 2015), affecting an onshore area >700 km^2 (Neri et al., 2004) and with a thickness of 1-4 km (Ruch et al., 2010; Siniscalchi et al., 2012; Ruch et al., 2012). This corresponds to the unstable flank delimited by the upper slip surface of Guardo et al. (2020), since this upper surface tends to emerge in correspondence of the Etna summit – NE Rift zone, and goes from above sea level down to almost 4 km b.s.l., from west to east. The unstable area also continues below sea level, until it reaches the abyssal plain at a depth of over 2000 meters (Urulaub et al., 2018). Several authors have recently highlighted the possible relationship between eruptive activity and flank deformation, showing that the acceleration of flank deformation may trigger flank eruptions and vice versa. In some cases, it was demonstrated that tectonic activity along the PFS triggers eruptions from the NE Rift (Neri et al., 2004, 2005; Walter et al., 2005; Bonforte et al., 2011; Ruch et al., 2012; De Novellis et al., 2019).

Applying the lithostratigraphic units following the standards suggested by Salvador (1994), two main groups of volcanic deposits are detectable in the NE Rift area (Fig. 3): the products belonging to the

Il Piano Synthem (Mongibello Volcano Lithosomatic Unit; 15,420±60 - 0 a BP) and those belonging to the Concazze Synthem (Ellittico volcano Lithosomatic Unit; 56.6±15.4 ka - 15,420±60 a BP) (Coltelli et al., 1994; Garduño at al., 1997; Coltelli et al., 2000). Both represent volcanic units made up of products erupted during the last ~57 ka and belonging to the Mongibello Supersynthem (Branca et al., 2011).

With reference to the stratigraphy in the bottom part of Figure 3, the Concazze Synthem coincides with Ellittico Volcano, a large stratovolcano with a main, summit eruptive vent approximately coinciding with the current summit of Etna, but higher (3600-3800 m a.s.l.). The stratigraphic succession consists of alternating lavas and pyroclastic deposits. It ends with plagioclase-rich porphyritic lava flows and reddish subaphiric lavas and scorias (Pizzi Deneri Formation and Portella Giumenta formation, respectively; Coltelli et al., 1994; Branca et al., 2011). The deposits of the final explosive activity at Ellittico date at 15,420±60 a BP (Condomines et al., 1982; Cortesi et al., 1988; Gillot et al., 1994; Coltelli et al., 2000; De Beni et al., 2011); this explosive activity also generated the formation of a large and deep summit caldera, whose remains today crop out at the edge of the highest portion of the NE rift, namely at Punta Lucia and Pizzi Deneri. In the NE-Rift area, the products of Portella Giumenta formation overlap deeply eroded cinder cones and porphyritic lavas belonging to Piano Provenzana formation.

The Il Piano Synthem constitutes the present active volcano. The lower boundary coincides with the Ellittico caldera, while the upper boundary is the current topographic surface. In the NE Rift, the volcanics belonging to the Pietracannone and Torre del Filosofo formations largely crop out. During the last 120 years, the NE Rift eruptions lasted 21 days on average, with 7 m^3s^{-1}eruption rates. The eruptive fissures reached in ~1 day the maximum length (3825 m) by propagating at an average speed of 0.053 ms^{-1} (Neri et al., 2011).

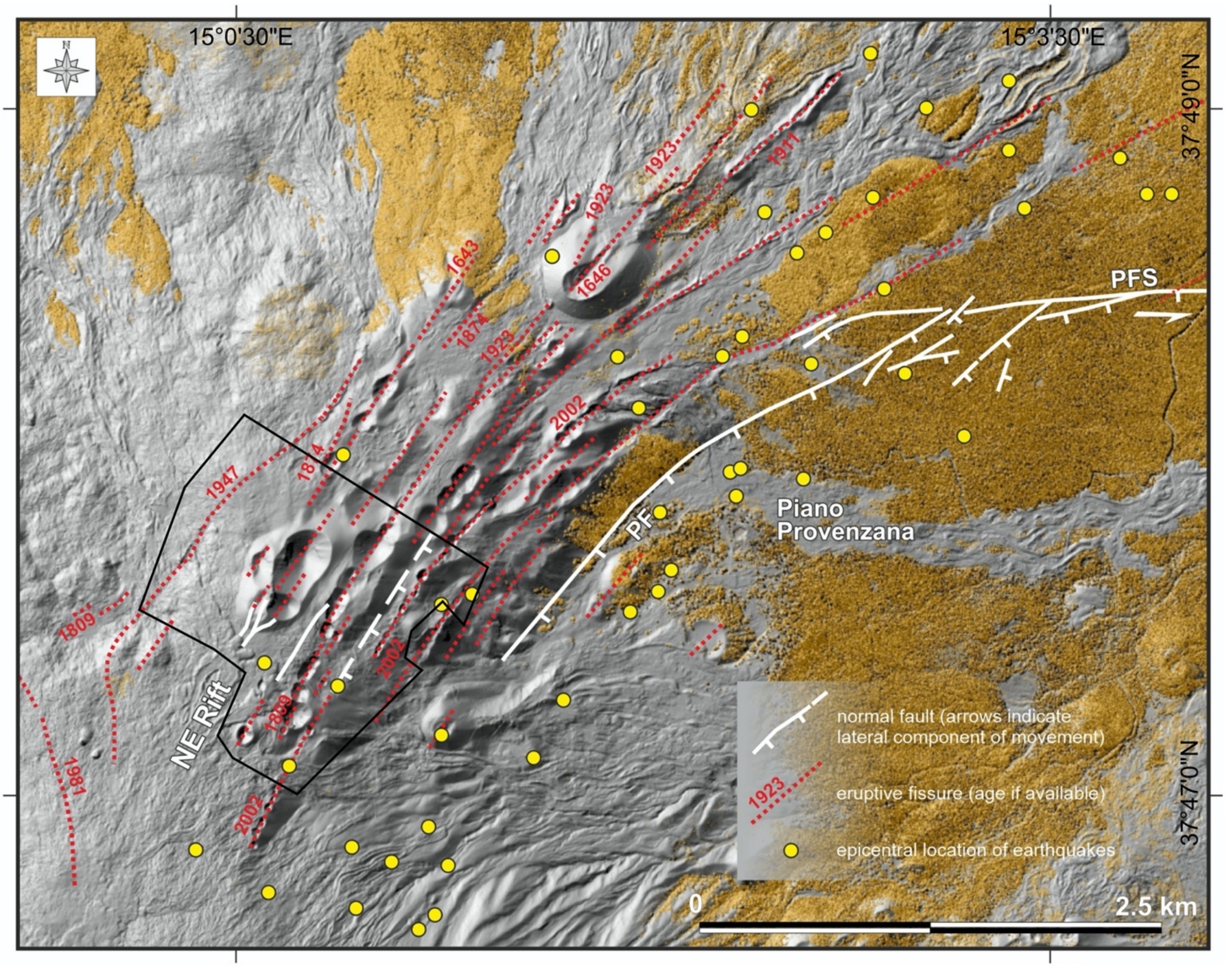

Figure 2. *Structural map of the NE Rift superimposed on a shaded relief Lidar derived image of the area. Numbers show date of historical eruptive fissures (dotted red lines), modified after Neri et al. (2004). Yellow circles mark the epicentral location of earthquakes recorded during the 2002-2003 eruption (for location error see caption of Fig. 1). In white major faults, PF: Piano Provenzana Fault, PFS: Pernicana Fault System. The area outlined by the black line represents the area of Figures 5-6 surveyed with the drones. The NE Rift is located in Figure 1.*

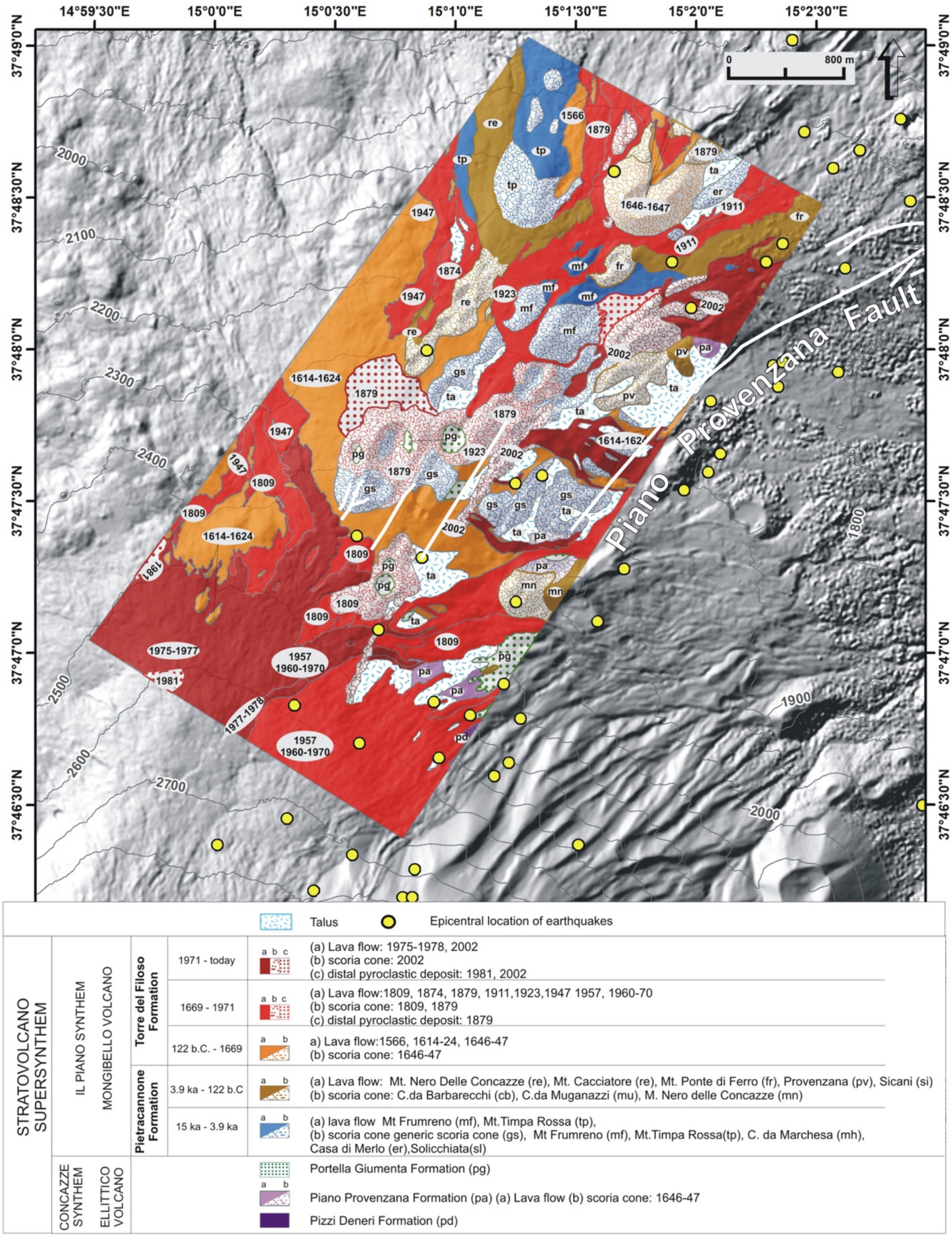

Figure 3. *Geological map of the NE Rift showing lithostratigraphic units, the 2002-2003 earthquake epicenters (yellow dots), and the main faults (in white), superimposed on a shaded relief DSM derived of the area (Gwinner et al., 2006). The NE Rift is located in Figure 1.*

3. Seismological data

Number of stations and geometry of the seismic network for the permanent monitoring of Etna significantly changed in the last 40 years. The boost of the seismic network (from five short period, vertical-component stations of the 1970s to the 30 broadband, 3-component sensors of 2020) has also involved signal transmission (from analogue to digital) and acquisition systems (Patanè et al., 2004). In the framework of seismic activity at Etna, the NE rift, along with the PFS and the PF, plays a key role. Indeed, they form a discontinuity that accommodates stress changes related to the magma intrusion and tectonic loading, interpreted as the main sources causing the eastward sliding of the eastern sector of the volcano (Alparone et al., 2013a,b).

The area of interest in this case study is situated at the westernmost part of the PFS-PF fault system. The structure has a bow-like geometry, striking NE at its western tip, and bending along an E-W strike direction towards east. Here the earthquakes are usually shallow (depths mostly between 0 and 3 km b.s.l.) and with small to moderate magnitude (< M_L 5) (Fig. 1C). Despite their magnitude, these superficial earthquakes can be damaging as documented by macroseismic studies, which highlight the high seismic hazard of this sector of the volcano (Azzaro et al., 1998; Azzaro, 2004). Alparone et al. (2013a,b) report that seismic activity at the PFS-PF fault system increased from September 2002 on, starting shortly (a month) before the 2002-2003 eruption. Overall, 874 earthquakes with Mmax 4.1 heralded the onset of that eruptive episode. Focusing on seismic activity during the 2002-2003 eruption, Mostaccio et al. (2013) tested NonLinLoc (Lomax et al., 2000), a nonlinear probabilistic earthquake location method, using a 3D velocity model. From the 328 well-constrained locations obtained by Mostaccio et al. (2013), we extracted a subset of 118 shallow earthquakes, which are located in an area encompassing the zone of our case study, part of the Valle del Bove and of the PFS-PF fault system. We used this 2002-2003 dataset because it contains the best located earthquakes and because it is representative of the typical seismic activity of this sector of Mt Etna. Figure 1C highlights a bow-shaped distribution of 90 epicentres starting from the summit caters. The striking correlation between epicentre location and structural elements is visible comparing Figure 1 and Figure 2, since both have an arcuate shape and seismicity recalls the bow shape of the faults and fracture distribution. Along the NE Rift, the earthquake distribution trends NNE-SSW, and tends to bend to NE-SW and E-W moving in eastern direction. This group of earthquakes is well separated from a second, smaller group (26) located more to the south, whose position clearly marks the northern rim of the Valle del Bove (Figure 1). It is worth noting that the peculiar distribution of earthquakes in Figure 1 is not only typical of the 2002-2003 eruptive period. Indeed, analysing the distribution of seismic foci during the years from 2000 to 2009 (with the exclusion of time spans with volcanic activity), Alparone et al. (2013a,b) identified a cluster of earthquakes, which closely marked the NE Rift and are aligned along the PFS-PF fault system. The magnitude of these earthquakes was small, with only two of them with M_L >2. A second cluster belonged to the easternmost sector of the PFS-PF; they had stronger magnitude, reaching values M_L 4.1.

Figure 1C depicts the fault plane solution calculated for the earthquakes reported in Table S1 (attached file), which occurred from 2008 to 2019 (source: http://sismoweb.ct.ingv.it/maps/eq_maps/focals/index.php). Even though the mechanisms show some scatter, common elements may be identified. The earthquakes located in the southwestern corner of the picture have T axes striking mostly N, NE and ENE. Most of these earthquakes have strike-slip or normal faulting mechanisms, with almost vertical P-axes. The earthquakes located in the northern part of the figure express the general trend of deformation along the PFS-PF fault system, with either normal faulting or horizontal strike-slip mechanism. All mechanisms of this group have T-axes striking in SE direction.

4. Methods

4.1 Drone survey, photo and GCPs collection

In the present work, we applied the Structure from Motion (SfM) photogrammetry techniques, through drone surveys, to build up the high-resolution Digital Surface Model (DSM) and Orthomosaic for the target area. We followed the overall workflow that has been successfully tested in volcanic terrains and in challenging logistic conditions (Bonali et al., 2019a, 2020). Such a workflow has been designed to work with commercial quadcopters over large areas in volcanic terrain, that is exactly the situation we tackled in the present work where we used the DJI Phantom 4 PRO. This device is supplied with an incorporated chipset to work with space-based satellite navigation/referencing system (GPS/GLONASS), and a high-resolution camera sensor (20 Megapixels) in order to enhance the quality of the surveying, as well as to obtain georeferenced pictures (Geographic coordinates/WGS84). The overall area has been surveyed by several different flight missions where each of them has been planned to consider the presence of natural obstacles - mainly identified as topographic highs - known from a previous field survey, topographic maps and satellite images. Flight height has been set up to 80-95 m above the ground, reaching the excellent pixel size of 2-3 cm for the resulting Orthomosaic. We set the flight path considering the wind speed and direction, and chose an overlap ratio of 85% and 80 %, along the flight path and in lateral direction, respectively (Gerloni et al., 2018; Antoniou et. al., 2019; Bonali et al., 2019a, 2020; Fallati et al., 2020). The constant speed velocity was set up by the app considering all above settings, and pictures have been captured using equal time interval modality.

As a parallel and complementary activity to the UAV survey, we collected several Ground Control Points (GCPs), distributed all over the area, essential to scale and reference the SfM-derived models, as well as to avoid any bulging effect (James and Robson, 2012; Turner et al., 2012; Westoby et al., 2012; Smith et al., 2016; Vollgger and Cruden, 2016; James et al., 2017; Esposito et al., 2017). We targeted 34 natural targets, as already successfully performed by Bonali et al. (2020), to speed up the GCPs collection avoiding the deployment and recovery of artificial targets. This method allowed us to save one day (8 hours) of fieldwork. All GCPs have been collected with the GPS/GNSS Stonex S850A multi-frequency receiver in RTK configuration (with sub-centimetre accuracy). Depending on the 3G network availability, the GPS was linked in real time with sicili@net network, a real-time correction service based on the caster NTRIP tool (http://193.206.223.39:5099/spiderweb/frmIndex.aspx) or, in base-rover configuration, data have been post-processed thanks to Stonex Cube manager using Monte Conca and Pizzi Deneri permanent station correction-data of the INGV network.

4.2 Photogrammetry processing

For the photogrammetry processing of the 4018 captured pictures, we used a commercial SfM software - Agisoft METASHAPE (http://www.agisoft.com/), which is commonly used due to the outstanding quality of the resulting output models (Cook, 2017; Burns and Delparte, 2017; Benassi et al., 2017). We also used the Agisoft Cloud beta service for data processing. The processing passed through some key steps (workflow), described in detail by Verhoeven (2011) and Brunier et al. (2016), which led to the realization of the DSM and the Orthomosaic as final products (see Fig. 4 and Tables 1-2), that are based on the SfM-derived sparse and dense clouds.

We divided the overall workflow in four principal steps: i) aligning of pictures, ii) georeferencing, iii) Dense Cloud generation, and iv) DSM and Orthomosaic production. A summary of all details regarding the photogrammetry processing and results are reported in Table 1 and 2.

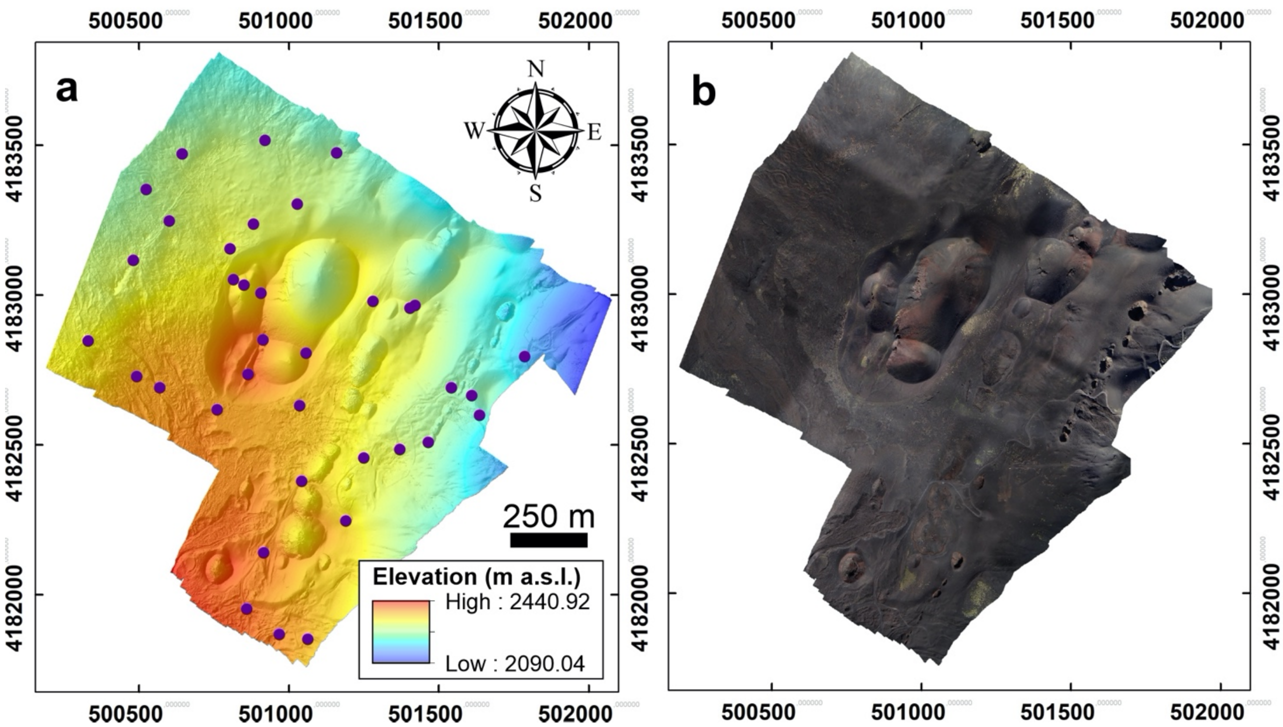

__Figure 4.__ Resulting DSM (a) and Orthomosaic (b) of the surveyed area, blue dots represent the location of surveyed GCPs. Ref. system: UTM33/WGS84.

__Table 1.__ Summary of setting and results related to the photogrammetry processing.

SfM Photogrammetry processing		
	Alignment processing settings	High accuracy / Generic and Reference Preselection
	Key Point / Tie Point limit	40,000 / 4,000
	Resulting Tie Points	1,773,948
	Dense Cloud processing settings	Medium Accuracy / Mild Filtering
	Resulting Dense Cloud (Points)	167,634,83
	Resulting DSM Resolution	11.86 cm/pix
	Resulting Orthomosaic	2.97 cm/pix

__Table 2.__ Outline of time production for DSM and Orthomosaic, including the time (in hh:mm:ss) for UAV survey and image collection.

UAV survey / Images Acquisition	SfM Photogrammetry Processing time							Overall total
	Tie Points		Depth maps	Dense Cloud	DSM	Orthomosaic	Total for SfM	
	Matching	Alignment						
3:07:00	1:18:00	0:40:06	7:11:00	2:06:00	0:14:18	1:50:00	13:19:24	16:26:24

4.3. Mapping and measurements gathering on SfM-derived models

The DSM and the Orthomosaic have been uploaded in a GIS environment, where we were able to trace all normal faults, extension fractures and eruptive fissures we recognized in the area (Fig. 5a).

Structures with a continuous vertical offset > 20 cm, as measured on the DSM, have been classified as normal faults, whereas structures with vertical offset < 20 cm have been classified as extension fractures. Regarding eruptive fissures, they have been traced considering morphometric parameters of the eruptive centres, as explained in Tibaldi (1995), Bonali et al. (2011) and Tibaldi and Bonali (2017): the strike of the feeding fracture is directly related to the elongation of the cone base and the crater, to the direction of the line connecting the depressions on the crater rim, and to the alignment of cones. In some eruptive centres, the outcropping dyke was visible, giving information about the direction and component of opening of the eruptive fissure.

On the base of the derived models, we collected a total of 574 structural data (432 at extension fractures and 142 at faults): on the DSM, we measured strike and vertical offset along the normal faults, by calculating the difference in elevation along topographic profiles traced every 10 m, orthogonally to the fault scarp. With regard to extension fractures, we determined the local strike, the opening direction vector and the amount of net dilation. The latter two values were obtained by tracing a line that connects the two piercing points located on the opposite sides of an extension fracture, whenever they were undoubtedly recognizable. The length of the line gives the net dilation and related opening vector.

Finally, along two NW-SE-trending transects traced parallel to the resulting overall direction of opening, the total amount of horizontal dilation has been calculated, cumulating each single value, as well as the extension rate and stretch in the area. These values were compared with the data collected in the field by Tibaldi and Groppelli (2002).

5. Results

We surveyed an area of 2.2 km^2 through the collection of a total of 4018 photos. Thanks to the above-described workflow, a high quality Orthomosaic and a DSM were reconstructed (Fig. 4), with a resulting ground resolution of 2.97 and 11.86 cm/pixel, respectively. On these models, we recognized the presence of 20 normal fault segments, 250 extension fractures and 54 eruptive fissures (Fig. 5a). The extension fractures strike mainly N20-50°, as highlighted in Figure 5b, with an average strike of N24.6°. Normal faults strike mainly N10-40° (Fig. 5c) with an average strike of N25.3°, whereas eruptive fissures strike mainly N20-40° (Fig. 5d) with an average strike of N29.8°. Regarding normal faults, they depict a graben running at the foothill of the westernmost pyroclastic cone, known as Monte Pizzillo (Fig. 5a). These faults have a maximum height of the SE-dipping scarp of 2.3 m (Fig. 6a), giving a heave of 0.6 m and assuming a fault plane dip of 75°. The fault scarp facing

NW reaches a height of 3 m giving a heave of 0.8 m. The fault scarp located towards the southeastern part of the studied area faces SE and reaches a maximum height of 4.2 m, resulting in a heave of 1.1 m.

To better understanding the active deformation processes affecting the area, we also collected a series of quantitative data at 144 sites along the extension fractures, totalling 432 structural measurements (Fig. 6). The latter include: *i)* local fractures strike; *ii)* the amount of fracture dilation; *iii)* the opening direction. Opening direction values are in the range N72-163°, with a mean value of N105.7°, and most values between N90-100° (rose diagram in Fig. 6b and Fig. 7a). The fracture strike compared with the fracture opening direction, highlights a clockwise rotation of fracture strike with the increasing in opening directions (Fig. 7a). We have also quantified the local extension fracture azimuth, obtaining values between N329.8°W and N78.8°, with a peak between N0-10° and a mean value of N19.1° (rose diagram in Fig. 6b), suggesting a slight overall left-lateral component of 3.4°. More in detail, the fractures with a lateral component < 5° were here classified as pure extensional fractures, whereas the remaining fractures have a left-lateral or a right-lateral component (Fig. 7b), counting 65 fractures with a left-lateral component, 40 fractures with a right-lateral component, and 39 pure extensional fractures, out of our 144 total data. Moreover, the component of left-lateral motions (up to 52°) is larger than the right-lateral component (up to 36°). The graph of Figure 7b also shows the relation between lateral components of motions and fracture azimuth: with an increase of the fracture strike, the lateral component tends to change from the right-lateral component to the left-lateral component.

The dilation values measured along extension fractures are in the range of 0.07-4.14 m (Figs. 6b and 7c), the average value is 0.4 m, and almost all values < 1 m. These values have been related to the local strike, showing that the greatest dilation values are associated to strike values of about N20°E; moving away from these strike values, dilation decreases gradually, especially if strike rotates in a NW-SE direction (Fig. 7e). Regarding structure length, extension fractures reach a maximum length of 93.8 m, with an average value of 13.8 m. Fractures with greater lengths show strike values between N40-60° E, decreasing gradually if strike rotates in an anticlockwise direction, and more abruptly if it rotates in a clockwise direction, as shown in Fig. 7f.

Regarding normal faults, we measured vertical offset every 10 meters along all the fault segments, obtaining values included in the range 0.1-7 m (Figs. 6a and 7d), the average value is 1.6 m and about half of the values < 1.5 m. Faults present greater lengths, reaching a maximum of 299.6 m, with an average value of 92.2 m (Fig. 7g). In particular, in Fig. 7g it is evident that greater lengths characterize SE-dipping faults, respect to NW-dipping ones, which are all < 85 m. Also, regarding the amount of displacement, we can observe that SE-dipping faults are characterized by greater values of offset than NW-dipping ones: the former reach a maximum offset of 7 m, whereas the latter reach a maximum value of 3 m (Fig. 7g). Regarding length/displacement ratios for normal faults, they are comprised between 11.3 and 284.7, with an average value of 67.9.

Considering a dip of 75° for normal faults, we were able to calculate the dilatational component at both extension fractures and normal faults. Thus, we determined the total extensional component along two transects (traces in Fig. 6a), both with a length of 1.43 km, oriented in the given overall spreading direction, obtaining a total value of 5.3 m in the northern part of the area, and of 7.6 m in the southern part, which correspond respectively to a stretching ratio of 1.003 in the north and 1.005 in the south.

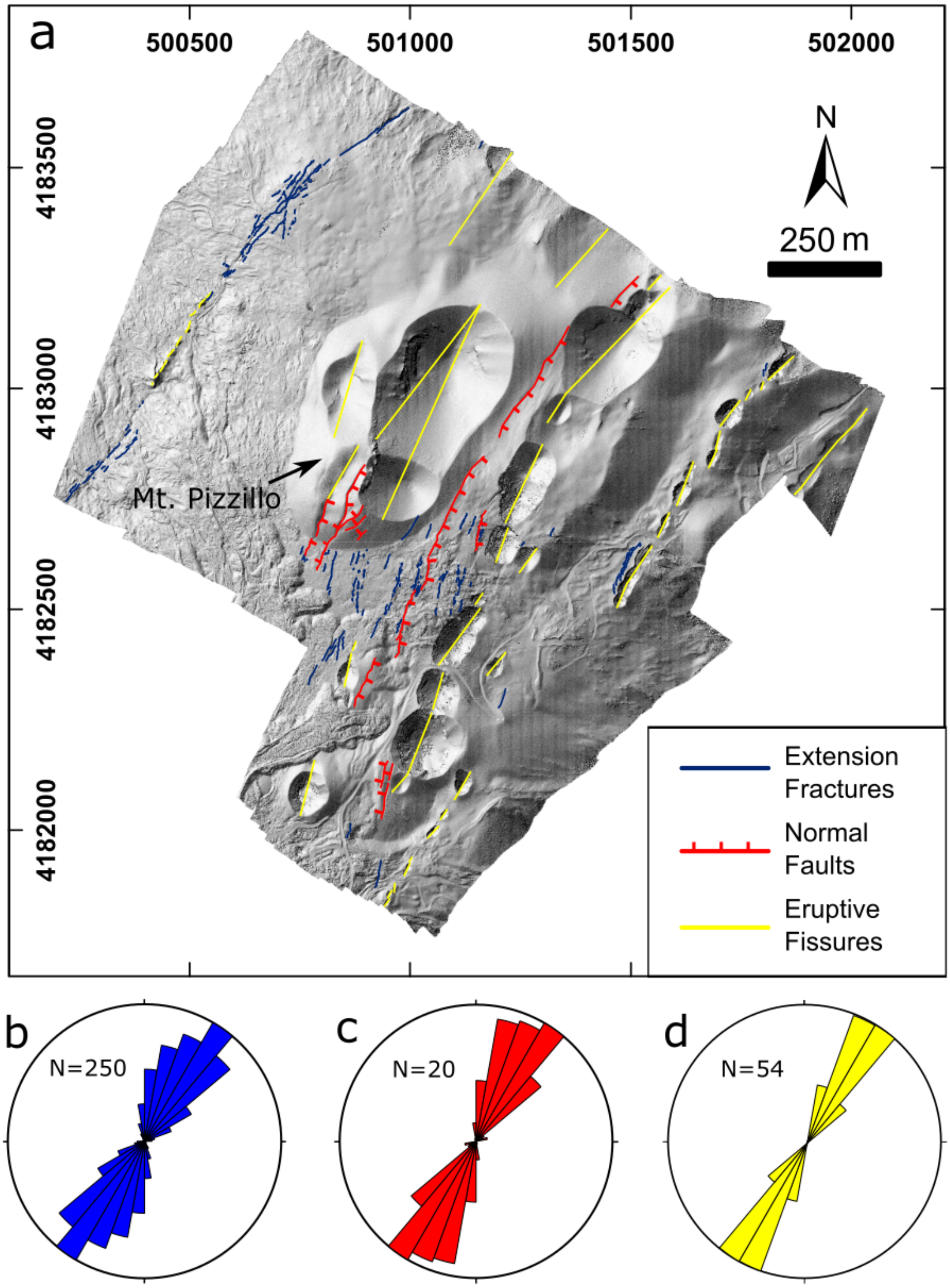

Figure 5. *(a) Geological-structural map of the studied area, structures are traced on high-resolution SfM-derived models, reference system: UTM33N-WGS84. Location in Figure 2. Rose diagrams show the strike of the extension fractures (b), normal faults (c) and eruptive fissures (d).*

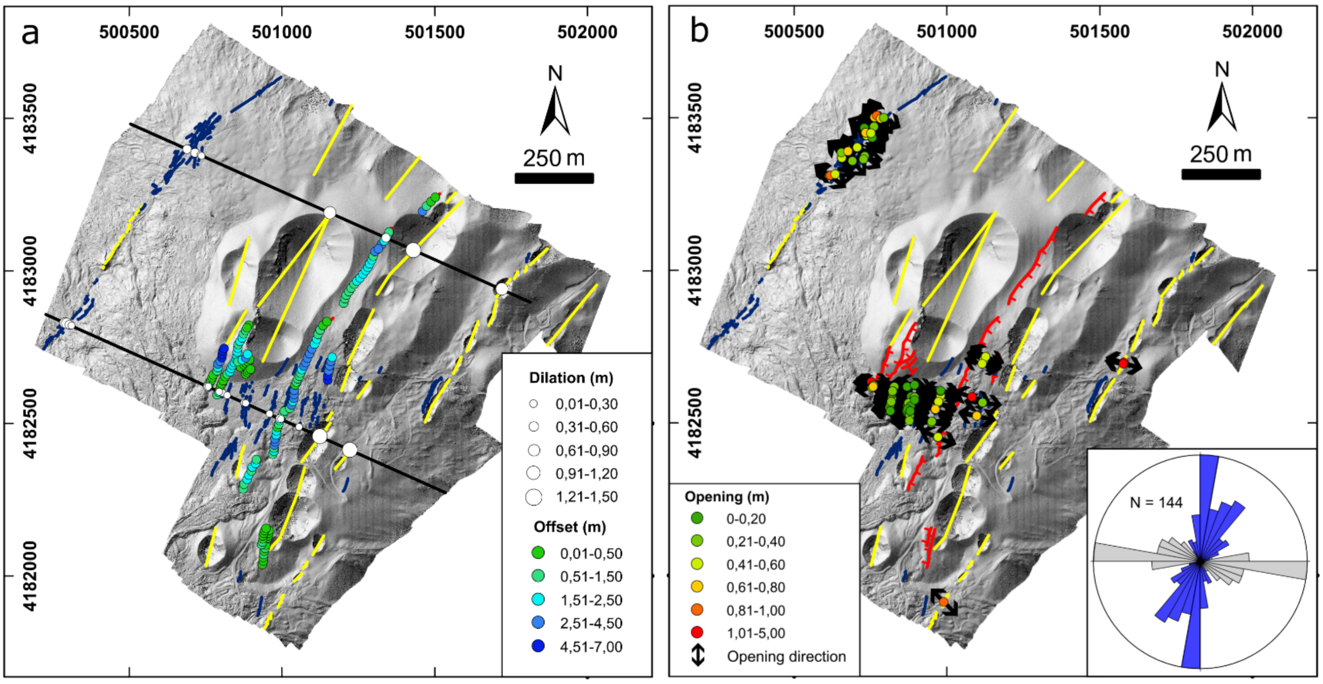

Figure 6. *Geological-structural map showing (a) vertical offset amounts along normal faults and values of horizontal dilation measured along the two transects (black lines = traces of the transects), (b) amount of opening and opening direction in the 144 detected structural stations. Rose diagram shows the distribution of net opening direction (grey) and of the respective local fracture azimuth (blue).*

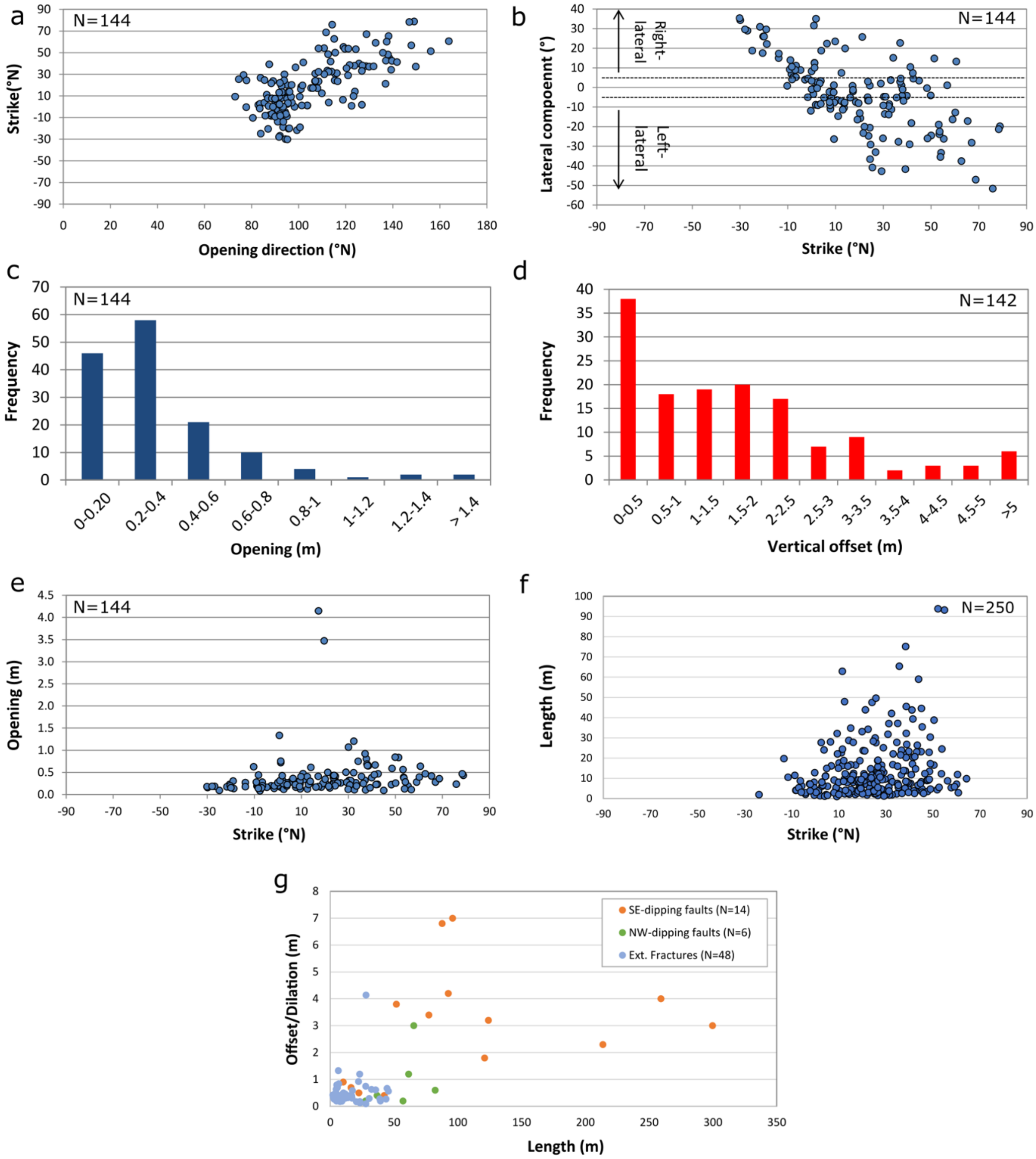

Figure 7. *(a) Graph comparing the local strike of extension fractures with the net opening direction at each site. (b) Graph comparing the local strike of extension fractures with the lateral component of motions at each site. (c) Histogram showing the frequency of the net dilation amount values measured along extension fractures. (d) Histogram showing the frequency of vertical offset values measured along normal faults. (e) Graph comparing the local strike of extension fractures with the net dilation amount at each site. (f) Graph comparing the strike of all the 250 extension fractures with their length. (g) Graph comparing the length of each structure with its maximum offset/dilation values, distinguishing between SE-dipping faults, NW-dipping faults and extension fractures.*

5. Discussion

5.1. Rift geometry, structuring and kinematics

The part of the rift where we focused our study belongs to the 4.5-km-long NE Rift of Mt Etna, a volcanotectonic feature that showed important volcanic and tectonic activity in historic times. The orientation of the structures surveyed by UAVs is coherent with the remaining structures of the central part of the NE Rift, which generally strike NE-SW. The remaining northeastern and southwestern portions of the NE Rift show a slight clockwise and counterclockwise rotation respect to the central part, giving to the rift a gentle concavity towards SE (Fig. 2). Most of the rift, and similarly the studied area, is dominated by extension fractures and a few normal faults. Among faults, the largest one is represented by the PF normal fault, facing SE, which constitutes the westernmost termination of the PFS (Groppelli and Tibaldi, 1999; Tibaldi and Groppelli, 2002; Acocella and Neri, 2005). Although the PFS has left-lateral strike-slip to transtensional motions, as shown by the focal mechanism solutions of Figure 1, in the studied sector the PF produces an escarpment, facing SE, about 200 m high that separates the ridge of the NE Rift from the flat plain of Piano Provenzana. This dominant downdip motion is linked to the rotation of the PFS-PF fault system that turns from an E-W orientation in the eastern part towards a NE-SW strike direction in the studied area. The other faults form small grabens, one of which is present in the studied sector: this graben is 35 m wide at the southwestern foothill of the Mt Pizzillo pyroclastic cone and widens up to 80 m in correspondence with the upper portions of the cone. We suggest that this geometry is mainly due to the interference between the fault dip and the shape of the conical edifice, as observed also at Mount Laki in Iceland (Trippanera et al., 2015) or along the Harrat Lunayyir fault in Saudi Arabia (Trippanera et al., 2019).

Regarding normal faults in the area, the calculated length/displacement ratios (11.3-284.7) are smaller than the ones obtained by Gudmundsson et al. (2013), which are in the range 42-362 (average about 130). Anyway, our work considered a very smaller area than the one studied by these authors, which studied all the principal faults of the eastern flank of the volcano, with lengths up to 12,950 m and displacements up to 190 m.

The 144 opening directions measured along the extension fractures on the images obtained by drone surveys and SfM, indicate a clear homogenous dominant extension vector trending N105.7°. This vector is perpendicular to the largest slope of the area that is represented by the scarp of the PF and coincides with the direction of maximum slope gradient of this part of Mt Etna (Favalli et al., 1999). As a consequence, we retain that the opening vector of the NE Rift is strongly influenced by gravity effects linked to the shape of the Mt Etna edifice. A comparison with seismicity indicates that here the focal mechanism solutions have T axes trending NW-SE (Fig. 1), consistent with the opening directions measured by the drone surveys.

The fact that the faults dipping to the SE are longer, have larger offsets, and are more frequent than those dipping to the NW, can be linked to the fact that the NE Rift has a strongly asymmetric profile measured in a NW-SE direction. Towards NW, in fact, there is a smooth topographic decrease, whereas in the opposite direction there is the steep slope gradient produced by the PF scarp. Moreover, the northwestern side of the NE Rift is buttressed by the stable northern volcano slope, whereas the southeastern side is involved in the gravity sliding of the eastern volcano slope. This means that there is a larger gravity force acting in the SE direction.

The fact that most opening took place at the fractures with a strike ranging N0-50°, and that the longest fractures strike N10-55°, can be explained assuming that this range corresponds to the local orientation of the opening vector linked with the instability of the eastern volcano flank. Finally, the generally larger values of length of faults respect to fractures is compatible with the concept that extensional fractures represent an immature stage of the evolution towards faults (Gudmundsson, 1987; Acocella et al., 2003; Tibaldi et al., 2019); faults can, in fact, derive from the linkage between different fracture segments during the evolutionary process.

Notwithstanding the general orthogonality of the opening direction respect to the average trend of the NE Rift, at a higher detail we observed that 45% of all extension fractures present a left-lateral component, whereas 27% are characterized by pure extension. Considering also that the component of left-lateral motions is larger than the right-lateral component, we conclude that the NE Rift has a left-lateral transtensional behaviour linked to the large strike-slip component of motions along the PFS.

Finally, we used the software “Lissage” (Lee and Angelier, 1994) and the unpublished software ATMO-STRESS, prepared in the framework of the NEANIAS project (https://www.neanias.eu/) of the E.U., to calculate the stress field. Lissage is a C-based software designed to reconstruct paleostress trajectories in a given area (Lee and Angelier, 1994), using as input data multiple local stress determinations, including P and T axes derived from seismological data, the direction of principal stress axes from stress inversion and any other data that describe the azimuth of σHMax/Min. Such software can be used to reconstruct stress trajectories both using local field data and regional paleostress database (e.g. Hu et al., 1996; Munoz-Martın et al., 1998; Maestro et al., 2007; Bonali et al., 2019b). The Lissage software was here used to quantify the stress field at a broader scale by the interpolation of σ_{hmin} resulting from T-axes of focal mechanism solutions and from the single points of measurement of net dilation direction at extension fractures in our study area (Fig. 8A), assuming that net dilation is parallel to σ_{hmin}. The ATMO-Stress software is the online version of such software, and was here used to calculate in detail, at a more local scale, the stress field based only on net dilation direction at extension fractures (Fig. 8B). Both results indicate a clear NW-SE trend of σ_{hmin}, although in detail it appears a slight anticlockwise rotation from East to West. We retain that this rotation is linked to the transition from the strike-slip dominion of the PFS, which strikes E-W, to the more extensional dominion of the rift-PF, which strike NE-SW.

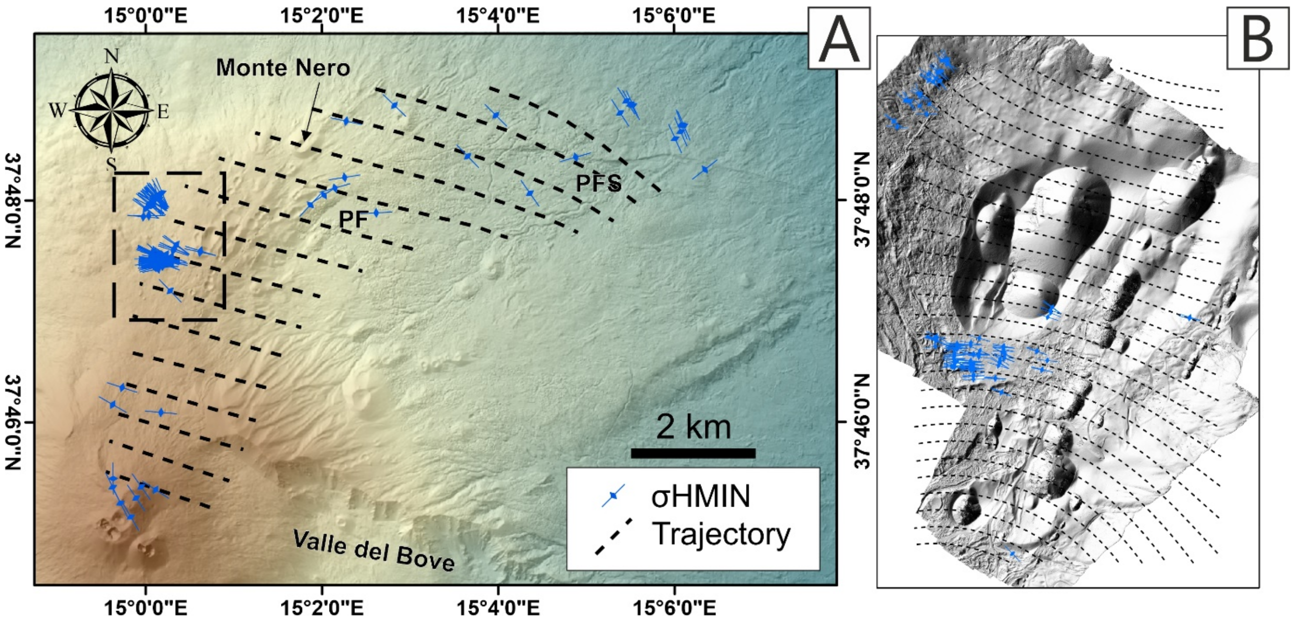

Figure 8. *Stress field trajectories obtained by the interpolation of σ_{hmin} in the whole NE rift (A) and in our study area (B). For stress computation, we used the program "Lissage" (Lee and Angelier, 1994) in (A), and the unpublished program ATMO-STRESS in (B).*

5.2. Extensional rate

The total extension measured along the faults and fractures that crop out in the studied area along the two transects, is of 5.3 m in the northern part of the area and of 7.6 m in the southern part. Assuming the age of 1614-1624 yr AD for the oldest lavas affected by the brittle structures, we obtain an extension rate of 1.87 cm/yr at the southern transect for the last 406 yr. Our measured extension rates are based on a wider dataset than that published in the Tibaldi and Groppelli (2002) paper, who indicated extension rates measured at single fractures with values of 1.8 cm/yr, 1.3 cm/yr, and 0.6 cm/yr along the rift moving from SW to NE. Our studied area corresponds to the southwestern portion of the NE Rift that, based on the data of Tibaldi and Groppelli (2002), opens at a higher rate. Our data thus indicate that this part of the rift opens at a slightly higher rate than previously suggested (1.87 cm/yr instead of 1.3-1.8 cm/yr) and we retain our result is based on a more robust statistical dataset.

This result is also coherent with the gross general rate of deformation measured along the nearest main structure that is represented by the PFS. This fault is linked to the NE Rift and this justifies its comparison with our data. The PFS slip-rate has been quantified in its central-western part at 0.4± 0.1 cm/yr to 2.2 ± 0.1 cm/yr, and in the eastern part at 0.2 ± 0.1 cm/yr to 0.8 ± 0.4 cm/yr where the PFS splays in the Vena-Presa zone (Tibaldi and Groppelli, 2002). The PFS short-term slip-rate has been assessed at 1 cm/yr in the vertical component and 2.8 cm/yr in the left-lateral component by Azzaro et al. (2001). A lower fault slip-rate of 0.6–1.5 cm/yr since 3 ka ago has been more recently calculated by D'Amato et al. (2017), although this refers only to the throw rate, not considering the strike-slip component that is especially high in the western and eastern part of the PFS. This consistency between the extension rate at the NE Rift and the slip along the PFS confirms that they accommodate the seaward sliding of the eastern volcano flank.

5.3. Methodological aspects

Results from the present work support the utility of using UAV-based SfM as a complementary tool to increase quality data collection, in addition to classical fieldwork, here aimed at defining the architecture and active processes working in a rift zone in volcanic areas. If we consider the time necessary to carry out the drone surveys, plus the time necessary to process the data and interpret them, we reach a total of 10 days of work. This yielded the collection of a huge amount of structural data, comprising 432 structural measurements (opening directions, amount of opening and local azimuth) at extension fractures. In comparison, Tibaldi and Groppelli (2002) collected just 22 opening directions in the field for the same area and related structural map over a total of one week of work.

The use of UAVs in geoscience is quickly increasing for a series of reasons: *i)* UAV data acquisition is cheaper respect to other methods, such as Airborne and terrestrial Laser Scanning, and LiDAR (Cawood et al., 2017; Lizarazo et al., 2017); *ii)* the proposed approach reduces work-time compared to field data collection, especially in the case of study of long structures as those of Tibaldi and Ferrari (1992), Kozhurin et al. (2006) and Trippanera et al. (2019); *iii)* the possibility to reach sites that can be inaccessible for logistic conditions or can be dangerous, such as an active volcano. Moreover, the excellent accuracy of the SfM-derived models allows us to carry out observations and measures at details in the order of cm, thus a scale that is comparable to field surveys. This scale, together with the velocity of the workflow and related processing, can even improve performance.

Furthermore, the rapid development of UAVs technology (furnished with Real-time kinematic positioning system) will increase the accuracy of the SfM outputs in the future, flying also at a higher elevation from the ground. Similarly, also the UAV flight stability, camera quality and battery capacity can improve thanks to the continuous delivery of new UAVs and related items.

In regard to limitations arising from the use of the UAV-based SfM, we mention the dependence on the flight time that is linked to the battery life, weather conditions, flight rules, and the fundamental step of placing and surveying the GCPs. The latter are needed to precisely scale and reference the model, but their placement is time consuming, slowing down the total time needed for the UAV missions, particularly over broad areas. Smith et al. (2016) suggested to consider a minimum 3 GCPs, whereas other authors considered a higher number of GCPs, but decreasing the overlap ratio among the pictures to 60-70% (Javernick et al., 2014). Finally, increasing overlap ratio, it is possible to decrease the number of GCPs considered for scaling and referencing (Esposito et al., 2017).

6. Conclusions

We applied UAV-based Structure-from-Motion (SfM) photogrammetry s to analyze a high-altitude area characterized by rough terrains in the northeastern part of Mt Etna. The area is affected by the presence of the NE Rift, a volcano-tectonic feature composed of NE-striking historic eruptive fissures, extension fractures and normal faults. The stratigraphic deposits span in age from 56.6 ± 15.4 ka BP to nowadays, whereas in the area surveyed by the drones, the deposits are mostly historic in age.

The highly detailed drone survey, in the order of 2.8 cm of resolution, showed that the studied sector of the NE Rift is affected by 250 extension fractures, 20 normal fault segments, and 54 eruptive fissures. The extension fractures strike mainly N20-50°, with an average strike of N24.6°. The normal faults strike mainly N10-40° with an average strike of N25.3°. The eruptive fissures strike mainly N20-40° with an average strike of N29.8°.

We measured 432 structural data, comprising local fracture strike, dilation amount, and opening direction. Opening direction values are in the range N72-163°, with a mean value of N105.7°. A comparison respect to fracture strike indicates the presence of a slight overall left-lateral component of 3.4°. Moreover, 65 fractures have a left lateral component, 40 fractures a right lateral component and 39 pure extension. The component of left-lateral motions (up to 52°) is larger than the right-lateral component (up to 36°). These data suggest the effect of the left-lateral normal Pernicana Fault System on the NE Rift kinematics.

Seismicity seems to be concentrated along the Pernicana-Piano Provenzana faults, whereas earthquake focal mechanism solutions show T-axes trending perpendicularly to the NE Rift, consistent with the results of our measurements of dilation orientations.

Assuming the age of 1614-1624 yr AD for the oldest lavas affected by the studied fractures, we obtain an extension rate of 1.87 cm/yr for the last 406 yr. This rate is consistent with the data measured by other authors at the Pernicana Fault System.

Results indicate that SfM photogrammetry coupled with drone surveys allows to collect large data sets with a detail comparable to field surveys. Drone survey has the advantage of collecting more data in the same time period respect to classical fieldwork, and also allows data collection in difficult terrains where logistics can represent an insurmountable obstacle.

Data availability:

Data are available from the corresponding author upon request.

Author contribution:

Conceptualization of the project was done by TA and CN. Photogrammetry processing of the 3D model was done by BFL. Data for the model and its calibration were collected and provided by CM, DBE, BFL and FL. Geological structural data and stratigraphy have been prepared by NM. Seismological data and text come from FS and LH. Evaluation of the model results and their interpretation were performed by CN and BFL. TA wrote the paper with help from all co-authors. All authors read and approved the final paper.

Competing interests:

The authors declare that they have no conflict of interest.

Acknowledgments: We acknowledge R. E. Rizzo and D. Trippanera for their useful suggestions to improve an earlier version of the manuscript. We are grateful to Tiziana Tuvè (INGV) for the data on hypocentral location of earthquakes in 2002-2003, and to Luciano Scarfì and Carmelo Cassisi for the access to http://sismoweb.ct.ingv.it/maps/eq_maps/focals/index.php. This study has been conducted in the framework of the EU project NEANIAS, within which the software ATMO-stress has been developed under the guidance of K. Karantzalos, the International Lithosphere Program - Task Force II (Leader A. Tibaldi), and it is also an outcome of: *i)* Project MIUR – Dipartimenti di Eccellenza 2018–2022; *ii)* GeoVires, the Virtual Reality Lab for Earth Sciences, Department of Earth and Environmental Sciences, University of Milan Bicocca, Italy (https://geovires.unimib.it/). We also acknowledge the Parco dell'Etna (https://parcoetna.it/) for permission for drone surveys.

References

Acocella, V., Neri, M. (2003). What makes flank eruptions? The 2001 Etna eruption and the possible triggering mechanisms. Bull. Volcanol., 65: 517-529, DOI: 10.1007/s00445-003-0280-3.

Acocella, V., Neri, M. (2005). Structural features of an active strike-slip fault on the sliding flank of Mt. Etna (Italy). J. Structural Geology, 27/2, pp. 343-355, doi: 10.1016/j.jsg.2004.07.006.

Acocella V, Neri M. (2009). Dike propagation in volcanic edifices: overview and possible developments, Special Issue: Gudmundsson – Volcanoes, Tectonophysics, 471, 67-77, doi: 10.1016/j.tecto.2008.10.002.

Acocella, V., Korme, T., Salvini, F., 2003. Formation of normal faults along the axial zone of the Ethiopian Rift. J. Struct. Geol., 25, 503–513.

Acocella V., Neri M., Sulpizio R. (2009). Dike propagation within active central volcanic edifices: constraints from Somma-Vesuvius, Etna and analogue models. Bull. Volcanol., 71:219–223, DOI 10.1007/s00445-008-0258-2.

Acocella V., Neri M., Norini G., (2013). An overview of analogue models to understand a complex volcanic instability: application to Etna, Italy, J. Volcanol. Geotherm. Res., 251, 98–111, doi:10.1016/j.jvolgeores.2012.06.003.

Acocella, V., Neri, M., Behncke, B., Bonforte, A., del Negro, C., & Ganci, G. (2016). Why does a mature volcano need new vents? The case of the New Southeast Crater at Etna. Frontiers in Earth Science, 4, 67. https://doi.org/10.3389/feart.2016.00067.

Alparone, S., A. Bonaccorso, A. Bonforte, and G. Currenti (2013a). Long-term stress-strain analysis of volcano flank instability: The eastern sector of Etna from 1980 to 2012, J. Geoph. Res., 118, 5098–5108, doi:10.1002/jgrb.50364, 2013.

Alparone. S., O. Cocina, S. Gambino, A. Mostaccio, S. Spampinato, T. Tuvè, A. Ursino, 2013b. Seismological features of the Pernicana–Provenzana Fault System (Mt. Etna, Italy) and implications for the dynamics of northeastern flank of the volcano. J. Volcanol. Geoth. Res., 251, 16–26, https://doi.org/10.1016/j.jvolgeores.2012.03.010.

Antoniou, V., Nomikou, P., Bardouli, P., Sorotou, P., Bonali, F., Ragia, L., Metaxas, A., 2019. The story map for Metaxa mine (Santorini, Greece): a unique site where history and volcanology meet each other. In Proceedings of the 5th International Conference on Geographical Information Systems Theory, Applications and Management, Heraklion, Greece, 3-5 May 2019; SciTePress, 1, 212–219.

Apuani T., C. Corazzato, A. Merri, & Tibaldi, A. (2013). Understanding Etna flank instability through numerical models, Journal of Volcanology and Geothermal Research, 251, 112- 126, doi: https://doi.org/10.1016/j.jvolgeores.2012.06.015.

Azzaro, R. (2004). Seismicity and active tectonics in the Etna region: constraints for a seismotectonic model, in Mt. Etna: volcano laboratory, Geophysical monograph (eds. A. Bonaccorso, S. Calvari,

M. Coltelli, C. Del Negro, S. Falsaperla), AGU, Washington D.C., 143, 205–220, doi:10.1029/143GM13.

Azzaro, R., L. Ferreli, A. L. Michetti, L. Serva, and E. Vittori (1998). Environmental hazard of capable faults: the case of the Pernicana fault (Mt. Etna, Sicily), Nat. Hazards, 17, 147–162.

Azzaro, R., Mattia, M., & Puglisi, G. (2001). Fault creep and kinematics of the eastern segment of the Pernicana Fault (Mt. Etna, Italy) derived from geodetic observations and their tectonic significance. Tectonophysics, 333(3-4), 401-415.

Behncke, B., Branca, S., Corsaro, R.A., De Beni, E., Miraglia, L. and Proietti, C. (2014). The 2011–2012 summit activity of Mount Etna: birth, growth and products of the new SE crater.J. Volcanol. Geotherm. Res. 270, 10–21.

Benassi, F., Dall'Asta, E., Diotri, F., Forlani, G., Morra di Cella, U., Roncella, R., Santise, M. (2017). Testing accuracy and repeatability of UAV blocks oriented with gnss-supported aerial triangulation. Remote Sens., 9, 172.

Bonali, F. L., Corazzato, C., & Tibaldi, A. (2011). Identifying rift zones on volcanoes: an example from La Réunion island, Indian Ocean. Bulletin of volcanology, 73(3), 347-366.

Bonali, F. L., Tibaldi, A., Marchese, F., Fallati, L., Russo, E., Corselli, C., Savini, A. (2019a). UAV-based surveying in volcano-tectonics: An example from the Iceland rift. J. Struct. Geol., 121, 46-64.

Bonali, F. L., Tibaldi, A., Mariotto, F. P., Saviano, D., Meloni, A., & Sajovitz, P. (2019b). Geometry, oblique kinematics and extensional strain variation along a diverging plate boundary: The example of the northern Theistareykir Fissure Swarm, NE Iceland. Tectonophysics, 756, 57-72.

Bonali, F. L., Tibaldi, A., Corti, N., Fallati, L., & Russo, E. (2020). Reconstruction of Late Pleistocene-Holocene Deformation through Massive Data Collection at Krafla Rift (NE Iceland) Owing to Drone-Based Structure-from-Motion Photogrammetry. Applied Sciences, 10(19), 6759.

Bonforte, A., Guglielmino, F., Coltelli, M., Ferretti, A., & Puglisi, G. (2011). Structural assessment of Mount Etna volcano from Permanent Scatterers analysis. Geochemistry, Geophysics, Geosystems, 12, Q02002. https://doi.org/10.1029/2010GC003213.

Borgia, A., Ferrari, L., & Pasquarè, G. (1992). Importance of gravitational spreading in the tectonic and volcanic evolution of Mount Etna. Nature, 357(6375), 231– 235.

Branca S., Coltelli M. & Groppelli G. (2011). Geological evolution of a complex basaltic stratovolcano: Mount Etna, Italy. It. J. Geosci. (Boll. Soc. Geol. It.), 130 (3), doi: 10.3301/IJG.2011.13.

Brunier, G., Fleury, J., Anthony, E. J., Gardel, A., Dussouillez, P. (2016). Close-range airborne Structure-from-Motion Photogrammetry for high-resolution beach morphometric surveys: Examples from an embayed rotating beach. Geomorphology, 261, 76-88.

Burns, J.H.R., Delparte, D. (2017). Comparison of commercial structure-from-motion photogrammetry software used for underwater three-dimensional modeling of coral reef environments. In: International Archives of the Photogrammetry, Remote Sensing and Spatial Information Sciences; ISPRS Archives, 42, 127–131.

Cappello, A., Neri, M., Acocella, V., Gallo, G., Vicari, A., Del Negro, C. (2012). Spatial vent opening probability map of Mt. Etna volcano (Sicily, Italy), Bull. Volcanol., 74, 2083–2094, doi: 10.1007/s00445-012-0647-4.

Cawood, A.J., Bond, C.E., Howell, J.A., Butler, R.W., Totake, Y., 2017. LiDAR, UAV or compass-clinometer? Accuracy, coverage and the effects on structural models. J. Struct. Geol., 98, 67-82.

Chu, D.; Gordon, R. G., 1999. Evidence for motion between Nubia and Somalia along the Southwest Indian Ridge. Nature, 398, 64-67, doi:10.1038/18014.

Cocina, O., Neri, G., Privitera, E., & Spampinato, S. (1997). Stress tensor computations in the Mount Etna area (Southern Italy) and tectonic implications. Journal of Geodynamics, 23(2), 109-127.

Cocina, O., Neri, G., Privitera, E., & Spampinato, S. (1998). Seismogenic stress field beneath Mt. Etna (South Italy) and possible relationships with volcano-tectonic features. Journal of volcanology and geothermal research, 83(3-4), 335-348.

Coltelli, M., Garduño, V.H., Neri, M., Pasquarè, G. & Pompilio, M. (1994). Geology of northern wall of Valle del Bove, Etna (Sicily). Acta Vulcanol., 5, 55-68.

Coltelli M., Del Carlo P. & Vezzoli L. (2000). Stratigraphic constrains for explosive activity in the last 100 ka at Etna volcano. Italy. Inter. J. Earth Sciences, 89, 665-677.

Condomines, M., Tanguy, J. C., Kieffer, G. & Allegre, C. J. (1982). Magmatic evolution of a volcano studied by 230Th-238U disequilibrium and trace elements systematics: the Etna case. Geochimica et Cosmochimica Acta, 46, 1397-1416. Pergamon Press Ltd. U.S.A.

Cook, K.L. (2017). An evaluation of the effectiveness of low-cost UAVs and structure from motion for geomorphic change detection. Geomorphology, 278, 195–208.

Cortesi, C., Fornaseri, M., Romano, R., Alessio, M., Allegri, L., Azzi, C., Bella, F., Calderoni, G., Follieri, M., Improta, S., Magri, D., Preite, Martinez M., Sadori, L., Petrone, V. & Turi, B. (1988). Cronologia 14C di piroclastiti recenti del Monte Etna identificazione e distribuzione dei fossili vegetali. Boll. Soc. Geol. It., 107, 531-545.

D'amato, D., Pace, B., Di Nicola, L., Stuart, F. M., Visini, F., Azzaro, R., Branca, S. & Barfod, D. N. (2017). Holocene slip rate variability along the Pernicana fault system (Mt. Etna, Italy): Evidence from offset lava flows. GSA Bulletin, 129(3-4), 304-317.

Darmawan, H., Walter, T.R., Brotopuspito, K.S., Nandaka, I.G.M.A. (2018). Morphological and structural changes at the Merapi lava dome monitored in 2012–15 using unmanned aerial vehicles (UAVs). J. Volcanol. Geotherm. Res., 349, 256-267.

De Beni E., Branca S., Coltelli M., Groppelli G. & Wijbrans J. (2011). 40Ar/39Ar isotopic dating of Etna volcanic succession. It. J. Geosci. (Boll. Soc. Geol. It.), 130 (3), 292-305, doi: 10.3301/IJG.2011.14.

De Beni, E., Cantarero, M., Messina, A. (2019). UAVs for volcano monitoring: A new approach applied on an active lava flow on Mt. Etna (Italy), during the 27 February–02 March 2017 eruption. J. Volcanol. Geotherm. Res., 369, 250-262.

De Novellis, V., Atzori, S., De Luca, C., Manzo, M., Valerio, E., Bonano, M., C. Cardaci, R. Castaldo, D. Di Bucci, M. Manunta, G. Onorato, S. Pepe, G. Solaro, P. Tizzani, I. Zinno, M. Neri, R. Lanari, F. Casuet (2019). DInSAR analysis and analytical modeling of Mount Etna displacements: The December 2018 volcano-tectonic crisis. Geophysical Research Letters, 46, doi.org/10.1029/2019GL082467.

Del Negro C., Cappello A., Neri M., Bilotta G., Hérault A., Ganci G. (2013). Lava flow hazards at Etna volcano: constraints imposed by eruptive history and numerical simulations, Scientific Reports - Nature, 3:3493, doi: 10.1038/srep03493.

Esposito, G., Mastrorocco, G., Salvini, R., Oliveti, M., Starita, P. (2017). Application of UAV photogrammetry for the multi-temporal estimation of surface extent and volumetric excavation in the Sa Pigada Bianca open-pit mine, Sardinia, Italy. Environ. Earth Sci., 76, 103.

Fallati, L., Saponari, L., Savini, A., Marchese, F., Corselli, C., Galli, P. (2020). Multi-Temporal UAV Data and Object-Based Image Analysis (OBIA) for Estimation of Substrate Changes in a Post-Bleaching Scenario on a Maldivian Reef. Remote Sens., 12, 2093.

Favalli, M., Innocenti, F., Teresa Pareschi, M., Pasquarè, G., Mazzarini, F., Branca, S., & Tibaldi, A. (1999). The DEM or Mt. Etna: geomorphological and structural implications. Geodinamica Acta, 12(5), 279-290.

Garduño V.H., Neri M., Pasquarè G., Borgia A., Tibaldi A., 1997. Geology of the NE-Rift of Mount Etna (Sicily, Italy). Acta Vulcanologica, 9, (1/2), 91-100.

Gerloni, I.G., Carchiolo, V., Vitello, F.R., Sciacca, E., Becciani, U., Costa, A., Riggi, S., Bonali, F.L., Russo, E., Fallati, L., Marchese, F., Tibaldi, A. (2018). Immersive Virtual Reality for Earth Sciences. In: Proceedings of the 2018 Federated Conference on Computer Science and Information Systems (FedCSIS) IEEE, Poznan, Poland, 9-12 September 2018, 527-534.

Geshi N. and Neri M. (2014). Dynamic feeder dyke systems in basaltic volcanoes: the exceptional example of the 1809 Etna eruption (Italy). Front. Earth Sci. 2:13. doi: 10.3389/feart.2014.00013.

Gillot, P.Y., Kieffer, G. & Romano, R. (1994). The evolution of Mount Etna in the light of potassium-argon dating. Acta Vulcanol., 5, 81-87.

Groppelli, G., and Tibaldi, A. (1999). Control of rock rheology on deformation style and slip-rate along the active Pernicana Fault, Mt. Etna, Italy. Tectonophysics, 305(4), 521– 537. doi.org/10.1016/S0040-1951(99)00035-9.

Guardo, R. A., De Siena, L., & Dreidemie, C. (2020). Mt. Etna feeding system and sliding flank: a new 3D image from earthquakes distribution in a customisable GIS. Front. Earth Sci., 8:589925, doi: 10.3389/feart.2020.589925

Gudmundsson, A. (1987). Geometry, formation and development of tectonic fractures on the Reykjanes Peninsula, southwest Iceland. Tectonophysics, 139, 295–308.

Gudmundsson, A., De Guidi, G., Scudero, S. (2013). Length–displacement scaling and fault growth. Tectonophysics, 608, 1298-1309.

Gwinner, K., Coltelli, M., Flohrer, J., Jaumann, R., Matz, K. D., Marsella, M., Roatsch T., Scholten F., Trauthan, F. (2006). The HRSC-AX Mt. Etna project: High-resolution orthoimages and 1 m DEM at regional scale. International Archives of Photogrammetry and Remote Sensing, XXXVI (Part 1), http://isprs. free. fr/documents/Papers/T05-23.

Hu, J. C., Angelier, J., Lee, J. C., Chu, H. T., & Byrne, D. (1996). Kinematics of convergence, deformation and stress distribution in the Taiwan collision area: 2-D finite-element numerical modelling. Tectonophysics, 255(3-4), 243-268.

James, M. R., Robson, S. (2012). Straightforward reconstruction of 3D surfaces and topography with a camera: accuracy and geoscience application. J. Geophys. Res. Earth Surf., 117, F03017, doi: 10.1029/2011JF002289.

James, M.R., Robson, S., d'Oleire-Oltmanns, S., Niethammer, U. (2017). Optimising UAV topographic surveys processed with structure-from-motion: ground control quality, quantity and bundle adjustment. Geomorphology, 280, 51-66.

Javernick, L., Brasington, J., Caruso, B. (2014). Modeling the topography of shallow braided rivers using Structure-from-Motion photogrammetry. Geomorphology, 213, 166–182.

Jestin, F., Huchon, P., Gaulier, J. M. (1994). The Somalia plate and the East-African Rift system—Present-day kinematics. Geophys. J. Int., 116, 637–654, doi:10.1111/j.1365-246X.1994.tb03286.x.

Keir, D., Ebinger, C. J., Stuart, G. W., Daly, E., Ayele, A. (2006). Strain accommodation by magmatism and faulting as rifting proceeds to breakup: Seismicity of the northern Ethiopian rift. J. Geophys. Res. Solid Earth, 111, B05314, doi:10.1029/2005JB003748.

Kozhurin, A., Acocella, V., Kyle, P. R., Lagmay, F. M., Melekestsev, I. V., Ponomareva, V., Rust D., Tibaldi A., Tunesi A., Corazzato C., Rovida A., Sakharovh A., Tengonciang A., Uyd H. (2006). Trenching studies of active faults in Kamchatka, eastern Russia: Palaeoseismic, tectonic and hazard implications. Tectonophysics, 417(3-4), 285-304.

Lanzafame, G., Neri, M., Coltelli, M., Lodato, L., & Rust, D. (1997). North-South compression in the Nit. Etna region (Sicily): spatial and temporal distribution. Acta Vulcanologica, 9, 121-134.

Lee, J. C., & Angelier, J. (1994). Paleostress trajectory maps based on the results of local determinations: the “Lissage” program. *Computers & Geosciences*, *20*(2), 161-191.

Lizarazo, I., Angulo, V., Rodríguez, J. (2017). Automatic mapping of land surface elevation changes from UAV-based imagery. Int. J. Remote Sens., 38, 2603–2622.
Lomax, A., J. Virieux, P. Volant, and C. Thierry-Berge (2000). Probabilistic earthquake location in 3D and layered models, in Advances in Seismic Event Location, C. H. Thurber and N. Rabinowitz (Editors), Kluwer Academic Publishers, Dordrecht/Boston/London, 101–134.
Lyakhovsky, V., Segev, A., Schattner, U., Weinberger, R., 2012. Deformation and seismicity associated with continental rift zones propagating toward continental margins. Geochem. Geophys. Geosyst., 13, Q01012, doi:10.1029/2011GC003927.
Maestro, A., Somoza, L., Rey, J., Martínez-Frías, J., & López-Martínez, J. (2007). Active tectonics, fault patterns, and stress field of Deception Island: a response to oblique convergence between the Pacific and Antarctic plates. Journal of South American Earth Sciences, 23(2-3), 256-268.
Mattia, M., Bruno, V., Caltabiano, T., Cannata, A., Cannavò, F., D'Alessandro, W., di Grazia, G., Federico, C., Giammanco, S., la Spina, A., Liuzzo, M., Longo, M., Monaco, C., Patanè, D., & Salerno, G. (2015). A comprehensive interpretative model of slow slip events on Mt. Etna's eastern flank. Geochemistry, Geophysics, Geosystems, 16, 635–658. https://doi.org/10.1002/2014GC005585.
Mostaccio, A., T. Tuvè, D. Patanè, G. Barberi, and L. Zuccarello (2013). Improving Seismic Surveillance at Mt. Etna Volcano by Probabilistic Earthquake Location in a 3D Model 103, 4, 2447–2459, doi: 10.1785/0120110202.
Müller, D., Walter, T.R., Schöpa, A., Witt, T., Steinke, B., Gudmundsson, M.T., Dürig, T. (2017). High-resolution digital elevation modeling from TLS and UAV campaign reveals structural complexity at the 2014/2015 Holuhraun eruption site, Iceland. Front. Earth Sci., 5, 59.
Munoz-Martın, A., Cloetingh, S. A. P. L., De Vicente, G., & Andeweg, B. (1998). Finite-element modelling of Tertiary paleostress fields in the eastern part of the Tajo Basin (central Spain). Tectonophysics, 300(1-4), 47-62.
Neri M., Acocella V., Behncke B. (2004). The role of the Pernicana Fault System in the spreading of Mount Etna (Italy) during the 2002-2003 eruption. Bull Volcanol, 66, 417-430, DOI: 10.1007/s00445-003-0322-x.
Neri M., Acocella V., Behncke B., Maiolino V., Ursino A. Velardita R. (2005). Contrasting triggering mechanisms of the 2001 and 2002-2003 eruptions of Mount Etna (Italy). J. Volcanol. Geotherm. Res., 144, 235-255, doi:10.1016/j.jvolgeores.2004.11.025.
Neri M., Acocella V., Behncke B., Giammanco S., Mazzarini F., Rust D. (2011). Structural analysis of the eruptive fissures at Mount Etna (Italy). Ann. Geophys., 54, 5, 464-479, doi: 10.4401/ag-5332.
Patanè, D., O. Cocina, S. Falsaperla, E. Privitera, and S. Spampinato (2004). Mt. Etna volcano: A seismological framework, in Mt. Etna Volcano Laboratory, A. Bonaccorso, S. Calvari, M. Coltelli, C. Del Negro, Falsaperla (Editors), American Geophysical Monograph 143, 147–165, AGU, Washington, D. C., https://doi.org/10.1029/143GM10.
Ruch J., V. Acocella, F. Storti, M. Neri, S. Pepe, G. Solaro, E. Sansosti (2010). Detachment depth of an unstable volcano revealed by rollover deformation: an integrated approach at Mt. Etna, Geophys. Res. Lett., 37, L16304, doi:10.1029/2010GL044131.
Ruch J., Pepe S., Casu F., Acocella V., Neri M., Solaro G., Sansosti E. (2012). How do rift zones relate to volcano flank instability? Evidence from collapsing rifts at Etna, Geophys. Res. Lett., 39, L20311, doi:10.1029/2012GL053683.
Ruch J., Pepe S., Casu F., Solaro G., Pepe A., Acocella V., Neri M., Sansosti E. (2013). Seismo-tectonic behavior of the Pernicana Fault System (Mt Etna): a gauge for volcano flank instability? J. Geophys, Res. Solid Earth, 118, 4398–4409, doi:10.1002/jgrb.50281.
Salvador A. (1994). International Stratigraphic Guide. GSA Salvador A. (Ed.), Boulder, 1-214.

Scarfì, L., A. Messina, C. Cassisi (2013). Sicily and Southern Calabria focal mechanism database: a valuable tool for the local and regional stress field determination, Ann. Geophys., 56, 1, D0109; doi:10.4401/ag-6109.

Siniscalchi A., Tripaldi S., Neri M., Balasco M., Romano G., Ruch J., Schiavone D. (2012). Flank instability structure of Mt Etna inferred by a magnetotelluric survey, J. Geophys. Res., 117, B03216, doi:10.1029/2011JB008657, 2012.

Smith, M.W., Carrivick, J.L., Quincey, D.J. (2016). Structure from motion photogrammetry in physical geography. Prog. Phys. Geogr., 40, 247–275.

Solaro G., Acocella V., Pepe S., Ruch J., Neri M., Sansosti E. (2010). Anatomy of an unstable volcano through InSAR data: multiple processes affecting flank instability at Mt. Etna in 1994-2008. J. Geophys.Res., 115, B10405, doi:10.1029/2009JB000820.

Tibaldi, A. (1995). Morphology of pyroclastic cones and tectonics. Journal of Geophysical Research: Solid Earth, 100(B12), 24521-24535.

Tibaldi, A., & Ferrari, L. (1992). Latest Pleistocene-Holocene tectonics of the Ecuadorian Andes. Tectonophysics, 205(1-3), 109-125.

Tibaldi, A., & Groppelli, G. (2002). Volcano-tectonic activity along structures of the unstable NE flank of Mt. Etna (Italy) and their possible origin. Journal of Volcanology and Geothermal Research, 115(3-4), 277-302.

Tibaldi, A., & Bonali, F. L. (2017). Intra-arc and back-arc volcano-tectonics: Magma pathways at Holocene Alaska-Aleutian volcanoes. Earth-Science Reviews, 167, 1-26.

Tibaldi, A., Bonali, F. L., Mariotto, F. P., Russo, E., & Tenti, L. R. (2019). The development of divergent margins: Insights from the North Volcanic Zone, Iceland. Earth and Planetary Science Letters, 509, 1-8.

Tibaldi, A., Bonali, F. L., Vitello, F., Delage, E., Nomikou, P., Antoniou, V., Becciani U., Van Wyk de Vries B., Krokos M., Whitworth, M. (2020). Real world-based immersive Virtual Reality for research, teaching and communication in volcanology. Bull. Volcanol., 82, 38.

Trippanera, D., Ruch, J., Acocella, V., Rivalta, E. (2015). Experiments of dike-induced deformation: insights on the long-term evolution of divergent plate boundaries. J. Geophys. Res. Solid Earth, 120(10), 6913-6942.

Trippanera, D., Ruch, J., Passone, L., Jónsson, S. (2019). Structural mapping of dike-induced faulting in Harrat Lunayyir (Saudi Arabia) by using high resolution drone imagery. Front. Earth Sci., 7, 168.

Turner, D., Lucieer, A., Watson, C. (2012). An automated technique for generating georectified mosaics from ultra-high resolution unmanned aerial vehicle (UAV) imagery, based on structure from motion (SfM) Point clouds. Remote Sens., 4, 1392-1410.

Urulaub, M., Petersen, F., Gross, F., Bonforte, A., Puglisi, G., Guglielmino, F., Krastel, S., Lange, D., & Kopp, H. (2018). Gravitational collapse of Mount Etna's southeastern flank. Science Advances, 4(10), eaat9700. https://doi.org/10.1126/sciadv.aat9700.

Verhoeven, G. (2011). Taking computer vision aloft–archaeological three-dimensional reconstructions from aerial photographs with photoscan. Archaeol. Prospect., 18, 67-73.

Villani, F., Pucci, S., Azzaro, R., Civico, R., Cinti, F. R., Pizzimenti, L., G. Tarabusi, S. Branca, C. A. Brunori, M. Caciagli, M. Cantarero, Cucci L., D'Amico S., De Beni E., De Martini P. M., Mariucci M. T., Messina A., Montone P., Nappi R., Nave R., Pantosti D., Ricci T., Sapia V., Smedile A., Vallone R. & Venuti A., 2020. Surface ruptures database related to the 26 December 2018, MW 4.9 Mt. Etna earthquake, southern Italy. Scientific data, 7(1), 1-9.

Vollgger, S.A., Cruden, A.R. (2016). Mapping folds and fractures in basement and cover rocks using UAV photogrammetry, Cape Liptrap and Cape Paterson, Victoria, Australia. J. Struct. Geol., 85, 168-187.

Walter, T.R., Acocella, V., Neri, M., Amelung, F. (2005). Feedback processes between magmatism and E-flank movement at Mt. Etna (Italy) during the 2002-2003 eruption. J. Geophys. Res., 110, B10205, doi:10.1029/2005JB003688.
Weismüller, C., Urai, J.L., Kettermann, M., Hagke, C.V., Reicherter, K. (2019). Structure of massively dilatant faults in Iceland: lessons learned from high-resolution unmanned aerial vehicle data. Solid Earth, 10(5), 1757-1784.
Westoby, M.J., Brasington, J., Glasser, N.F., Hambrey, M.J., Reynolds, J.M. (2012). 'Structure-from-Motion' photogrammetry: a low-cost, effective tool for geoscience applications. Geomorphology, 179, 300–314.